J. Fluid Mech. (1997), *vol.* 341, *pp.* 1–18. Printed in the United Kingdom

Topographic stress parameterization in a quasi-geostrophic barotropic model

By WILLIAM J. MERRYFIELD AND GREG HOLLOWAY

Institute of Ocean Sciences, PO Box 6000, Sidney, BC V8L 4B2, Canada

(Received 1 December 1995 and in revised form 15 December 1996)

The physical basis for parameterizing topographic stress due to unresolved eddies is examined in a quasi-geostrophic barotropic model. Topographic stress parameterization is shown to represent two effects of eddies: attraction of the flow to a statistical equilibrium featuring topographically correlated mean currents, and dissipation of potential enstrophy. Performance is evaluated by comparing parameterized low-resolution models with explicit high-resolution models.

1. Introduction

The interaction of currents with bottom topography generates stresses (i.e. correlations of pressure with bottom slope) that can significantly influence ocean circulation. Such stresses tend to drive mesoscale mean flows along isobaths with the sense of anticyclonic circulation over topographic elevations (Haidvogel & Brink 1986; Holloway 1987; Treguier 1989). Topographic stress appears to be under-represented in ocean circulation models, whose resolution is limited by finite computing resources. Such models exhibit poleward eastern boundary currents, equatorward western boundary undercurrents, and cyclonic subpolar gyres that are too weak relative to observations (e.g. Eby & Holloway 1994).

Holloway (1992) suggested that these deficiencies arise from inadequate resolution of eddies that generate topographic stress. A simple parameterization was proposed which replaces the usual viscous operator, restoring horizontal velocity $\boldsymbol{u}$ toward rest, with one that restores $\boldsymbol{u}$ toward a topographically correlated flow $\boldsymbol{u}^*$, determined from inviscid barotropic theory.

Although the underlying basis for this parameterization has not been established confidently, its effect has been examined in several ocean circulation studies. These include a global ocean model (Eby & Holloway 1994), as well as regional studies of the Mediterranean (Alvarez *et al.* 1994), Japan Sea (Holloway, Sou & Eby 1995), Caribbean (Sou, Holloway & Eby 1996), and Strait of Georgia (Fyfe & Marinone 1995). The topographic stress parameterization yields apparent improvements in model fidelity, especially near continental margins. Model skills have been quantified by comparing with data from a global inventory of current meters (Holloway & Sou 1995).

Until given a firmer physical basis, the use of the topographic stress parameterization remains uncertain. This paper is an initial effort to examine the subgrid-scale processes represented by the parameterization, and to assess the importance of incorporating these effects in low-resolution models. Two effects are discussed. The first is a tendency for relaxation toward statistical equilibria featuring topographically correlated mean currents. The second is the concentration of potential enstrophy dissipation at small scales, relative to dissipation of energy. This effect is accentuated by topography,

because viscosity acting on topographically driven mean currents generates potential enstrophy on the larger scales. Unless the subgrid-scale dissipation is restored, potential enstrophy becomes too large, and the mean currents too weak.

We assess the performance of the parameterization in idealized coarse-resolution models. While such models omit small-scale details, we hope that they accurately represent the large-scale flows. The skill of low-resolution models is evaluated by comparing against results of high-resolution models on the mutually resolved scales. The high-resolution models exhibit prominent topographically correlated steady flows on the larger scales. Low-resolution models using the topographic stress parameterization accurately reproduce the form and strength of these flows. By contrast, models using eddy viscosity parameterizations yield steady flows that are distorted and too weak.

This initial investigation is based on a much-simplified model, consisting of quasi-geostrophic barotropic flow on a square doubly-periodic *f*-plane, over random topography. In addition, our model is forced stochastically, whereas the oceans are subject to mean forcing by buoyancy and wind stress. However, the mean-flow tendency considered here persists in models that include stratification and mean forcing (Treguier & McWilliams 1990) as well as finite-amplitude topography (Griffa *et al.* 1996). To establish a confident basis for parameterizing topographic stress in more realistic models will require further effort.

Properties of topographically driven mean flows are reviewed briefly in §2. The tendency for topographic stress to restore the flow toward statistical equilibrium is examined in §3. In §4, we discuss the role of the topographic stress parameterization in dissipating potential enstrophy. The performance of the parameterization is evaluated in §5. Rationales for choosing parameters are considered in §6, and conclusions presented in §7.

2. Properties of topographically driven flows

Eddies interacting with bottom topography give rise to systematic stresses, driving large-scale mean flows (Holloway 1987). A starting point is the barotropic potential vorticity equation,

$$\frac{\partial q}{\partial t}+J(\psi,q)=F-D, \tag{1}$$

where ψ is the streamfunction, $J(A,B)=|\partial(A,B)/\partial(x,y)|$ is the Jacobian determinant with respect to the horizontal coordinates (x,y), F represents torques due to wind stress, and D is a dissipation operator. For constant Coriolis parameter f and bottom topography described by $h=f(H_o-H)/H_o$, where $H(x,y)$ is depth with mean H_o, potential vorticity is

$$q=\zeta+h, \tag{2}$$

where $\zeta=\nabla^2\psi$ is relative vorticity. For the doubly periodic *f*-plane considered here, the flow can be expanded in a Fourier series with respect to wave vector $\boldsymbol{k}$.

2.1. *Inviscid flow*

Solutions for statistical equilibria of (1) and (2) are available in the inviscid limit $F=D=0$. The continuum version of (1) then conserves arbitrary functions of q integrated over the domain. When the domain is discretized, the surviving invariants are energy,

$$E=\frac{1}{2}\iint(\boldsymbol{\nabla}\psi)^2\,\mathrm{d}x\,\mathrm{d}y, \tag{3}$$

potential enstrophy,

$$Q = \frac{1}{2}\iint q^2 \,\mathrm{d}x\,\mathrm{d}y, \tag{4}$$

and circulation, $C = \iint \zeta \,\mathrm{d}x\,\mathrm{d}y$, where $C = 0$ in the doubly periodic geometry considered here.

The existence of invariants E and Q enables the use of equilibrium statistical mechanics to determine stationary statistics. By such means, Salmon, Holloway & Hendershott (1976) found that the mean streamfunction is described by $\mu\bar{\psi} = \bar{q}$, or, in terms of its Fourier components,

$$\bar{\psi}_{\boldsymbol{k}} = \frac{h_{\boldsymbol{k}}}{\mu + k^2}, \tag{5}$$

where $\mu \equiv a/b$ is the ratio of two Lagrange multipliers, defined through the relations

$$E = \frac{1}{2}\sum_{k=k_0}^{k_1} \frac{1}{a+bk^2} + \frac{k^2|h_{\boldsymbol{k}}|^2}{((a/b)+k^2)^2}, \tag{6}$$

$$Q = \frac{1}{2}\sum_{k=k_0}^{k_1} \frac{k^2}{a+bk^2} + \frac{(a/b)^2|h_{\boldsymbol{k}}|^2}{((a/b)+k^2)^2}, \tag{7}$$

where k_0 and k_1 are the fundamental and truncation wavenumbers, and $k = |\boldsymbol{k}|$. The bars denote quantities associated with the mean component of flow, averaging over an ensemble of solutions having the same E and Q, but different random initial conditions. In statistical equilibrium, this is equivalent to temporal averaging, provided that the system is ergodic, i.e. that it occupies with equal probability all configurations accessible to it under conservation of E and Q.

The statistical mechanical treatment described above is based upon conservation of E and Q. Recent efforts (Miller 1990; Robert & Sommeria 1991) have extended statistical mechanical methods to account for additional invariants, for example revealing how coherent vortices can form from layers of uniform shear (Sommeria, Staquet & Robert 1991). Results based only on E and Q suppose that initial conditions are nearly maximally random within the constraints of given second-order correlations. This is indeed the case for the initial conditions (random phases and amplitudes scaled by prescribed spectra) considered here.

2.2. *Unforced viscous flow*

Asymptotic solutions are available also for $F = 0$, with D representing weak dissipation acting primarily at high wavenumbers (Bretherton & Haidvogel 1976). Under such conditions, Q is presumed to dissipate much more rapidly than E, and the flow is approximately that having minimum Q for a given E. The streamfunction is again given by (5), but in this instance the flow is entirely steady, unlike the inviscid case. Carnevale & Frederiksen (1987) show that these two regimes become equivalent in the limit of infinite resolution.

2.3. *Forced–dissipative flow*

Neither of the above limits corresponds to the circumstance $F \neq 0$ relevant to the oceans. For this case, no simple analytical descriptions are known. However, some conclusions can be drawn from numerical solutions of (1). The timescale for inviscid solutions to relax to statistical equilibrium is that characterizing the nonlinear interactions, $t_e \sim \zeta_{rms}^{-1}$, where ζ_{rms} is the root-mean-square relative vorticity. Numerical

Parameter		Value
Domain	L	1280 km
Grid size	N	256
Grid resolution	L/N	5 km
Cutoff wavenumber	k_1/k_0	85
Bottom friction	ν_0	10^{-7} s^{-1}
Biharmonic friction	ν_4	8.6×10^{15} cm^4 s^{-1}
Mean ocean depth	H_0	5000 m
Topographic relief (r.m.s.)	$(H_0-H)/H_0$	0.05
Coriolis parameter	f	10^{-4} s^{-1}
Forcing timescale	τ_F	1.8 days

TABLE 1. Parameters common to models R1 and R2

experiments have shown that when dissipation is present, the entropy maximization tendency still is prevalent, provided that $t_e \ll t_\nu$, where t_ν is the viscous decay timescale (Zou & Holloway 1994). For the oceans, t_e is roughly the turnover timescale of the energetic mesoscale eddies. For 100 km, 10 cm s^{-1} eddies, $t_e \sim 10^6$ s $\sim$ 10 days. A timescale t_ν estimated from quadratic bottom drag with abyssal velocity 3 cm s^{-1}, drag coefficient 1.3×10^{-3}, and 3000 m depth implies $t_\nu \sim 2$ years. An estimate based upon dissipation of vertical shear, with vertical viscosity 10 cm^2 s^{-1} and currents extending 300 m in depth, yields a comparable t_ν. The limit $t_e \ll t_\nu$ therefore appears to be applicable.

We suppose here that F fluctuates randomly in time, with zero mean. Such forcing maintains the flow against viscous decay, but does not itself directly drive mean currents. Provided $t_e \ll t_\nu$, one guesses that the entropy maximization tendency will be manifest, and that the steady component of flow will be described by (5). Previous numerical experiments (e.g. Treguier 1989) have demonstrated this approximate proportionality between $\bar{\psi}$ and $\bar{q}$.

The experiments described here illustrate the influence of topographic stress on forced-dissipative barotropic flow, and will serve later to assess the performance of subgrid-scale parameterizations. Numerical solutions are obtained by Fourier spectral collocation, dealiased by the 2/3 rule (e.g. Canuto *et al.* 1988). Temporal integration is via a second-order partially corrected Adams–Bashforth scheme, which does not suffer the time-splitting instability of the leapfrog scheme (Gazdag 1976). Random homogenous topography is generated by selecting complex spectral coefficients from a bi-Gaussian distribution, scaled according to a one-dimensional power spectrum $\propto (k+4k_0)^{-2.5}$.

For the dissipation operator D we choose a bottom friction plus a biharmonic lateral friction,

$$D_k = -(\nu_0+\nu_4 k^4)\,\zeta_k. \tag{8}$$

The random forcing is described by a Markov process, with

$$\partial F_k/\partial t = -\frac{1}{\tau}F_k + G_k(t), \tag{9}$$

where $G_k(t)$ is a white noise process, and τ is a forcing timescale. The $G_k(t)$ are selected from a bi-Gaussian distribution with power spectrum $\propto \exp[-(k-3k_0)^2/k_0^2]$ over $k_0 < k < 5k_0$. By restricting forcing to the largest scales, we simplify subsequent analysis of how performance varies with resolution.

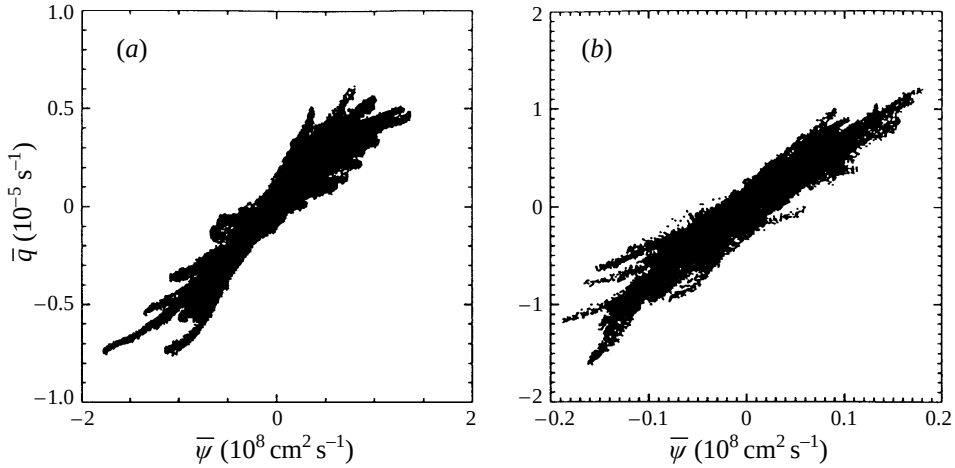

FIGURE 1. Scatter plots of mean streamfunction $\bar{\psi}(x, y)$ and potential vorticity $\bar{q}(x, y)$ for (*a*) model R1, and (*b*) model R2.

Quantity	R1	R2
r.m.s. F (10^{-12} s^{-2})	0.77	0.10
$\bar{E}$ (cm^2 s^{-2})	57.1	2.2
$\bar{Q}$ (10^{-12} s^{-2})	5.9	9.4
μ (units of k_0^2)	19.6	294
$E^{(m)}/\bar{E}$	0.666	0.563
t_e (days)	3.2	7.2
t_v (days)	114	101

TABLE 2. Properties of models R1 and R2

We consider two models in which the resolution ($k_1 = 85k_0$) is sufficient that further increase has little effect. (Models with $k_1 = 171k_0$ and similar forcing and dissipation behave in much the same way.) By considering two examples, we gain confidence that our results are reasonably general. Statistical equilibria are achieved within six months or so, and temporal means are evaluated during subsequent averaging periods of approximately five years. Some parameters common to both models are listed in table 1. The two models, R1 and R2, differ in amplitude of forcing, and hence in mean energy $\bar{E}$, as summarized in table 2. (Hereafter, we shall use $\bar{E}$ to denote mean energy, $E^{(m)}$ to denote energy of the mean flow, and $E^{(f)} = \bar{E} - E^{(m)}$ to denote the energy of the fluctuating flow, with similar conventions for Q.) Model R1 is more energetic, with an r.m.s. velocity of 10.7 cm s^{-1}, as compared to 2.1 cm s^{-1} for model R2. These values reflect a range of velocities encountered in the open oceans. Note that although model R1 is more energetic than R2, its mean potential enstrophy Q is smaller. This is because of the higher relative vorticity ζ in R1, together with the tendency for ζ to be anticorrelated with topography h. In both models, the mean-flow energy $E^{(m)}$ comprises more than half the total mean energy $\bar{E}$.

Figures 1 and 2 illustrate properties of model R1. In figure 1, the approximate linearity between $\bar{\psi}$ and $\bar{q}$ is evident. (The values of μ in table 2 are computed by linear regression fits to such distributions.) Figure 2(*a*) shows the random topography h, interpolated to a 64×64 grid for clarity, and figure 2(*b*) shows $\bar{\psi}$, which is correlated with h in accordance with (5). The energy spectra of the mean and fluctuating flows are

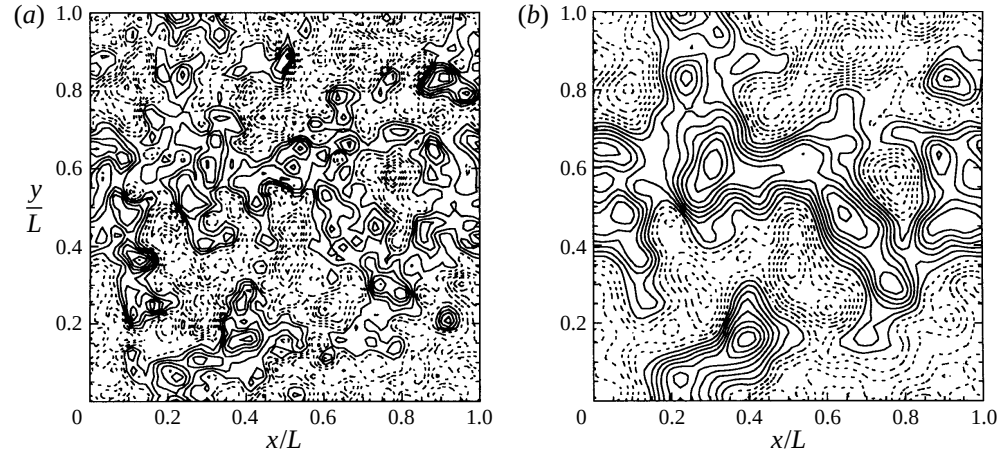

FIGURE 2. For model R1, (*a*) bottom topography h, and (*b*) mean streamfunction $\bar{\psi}$. For clarity, contributions from wavenumbers higher than $k = 32$ are filtered from h.

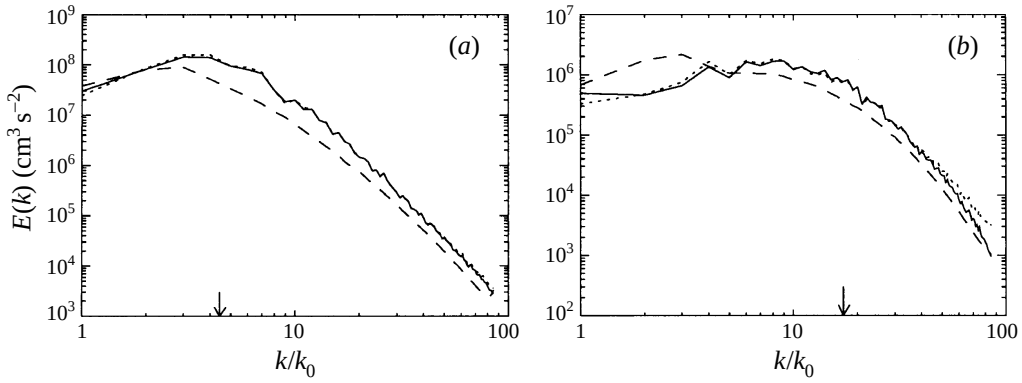

FIGURE 3. Energy spectra for models (*a*) R1, and (*b*) R2. Solid lines: mean-flow energy $E^{(m)}$. Dashed lines: fluctuating-flow energy $E^{(f)}$. Dotted lines: mean-flow energy spectrum implied by (5), with μ determined from scatter plots such as figure 1. Arrows indicate the wavenumbers $\mu^{1/2}$.

shown in figure 3. The mean-flow energy spectrum (solid line) closely follows that of the topographically correlated flow (dotted line) implied by (5). The exception is for wavenumbers $k \gtrsim 60k_0$ in R2, where biharmonic friction evidently damps the mean flow.

3. Topographic stress and restoration of equilibrium

The equilibrium statistical mechanics of inviscid flows was summarized in §2.1. Properties of such flows away from equilibrium are less well known, although some general statements can be made. Because entropy S is maximum at equilibrium, departures from equilibrium lead to decreased S (Carnevale 1982). For mean system properties described by parameters ϕ_n, $n = 1, \ldots, N$, a Taylor series expansion about equilibrium has linear terms which vanish, so that

$$S(\phi_1, \ldots, \phi_N) \approx S(\phi_1^*, \ldots, \phi_N^*) + \frac{1}{2}\sum_{nj}\left(\frac{\partial^2 S}{\partial\phi_n\,\partial\phi_j}\right)^* (\phi_n - \phi_n^*)(\phi_j - \phi_j^*), \tag{10}$$

where the asterisks denote equilibrium properties. Consider the temporal behaviour of the ensemble mean parameters $\overline{\phi_n}$. At equilibrium, $\mathrm{d}\overline{\phi_n}/\mathrm{d}t$ vanishes, as does $\overline{\partial S/\partial \phi_n}$. Near equilibrium, one expects $\mathrm{d}\overline{\phi_n}/\mathrm{d}t$ and $\overline{\partial S/\partial \phi_n}$ to depend linearly upon the departure $\overline{\phi_n}-\phi_n^*$, hence

$$\begin{aligned}\frac{\mathrm{d}\overline{\phi_n}}{\mathrm{d}t} &= \sum_l \alpha_{nl} \frac{\overline{\partial S}}{\partial \overline{\phi}_l} \\ &= \sum_{jl} \alpha_{nl} \left(\frac{\overline{\partial^2 S}}{\partial \overline{\phi}_l \partial \overline{\phi}_j} \right)^* (\overline{\phi_j} - \phi_j^*) \\ &= -\sum_j K_{nj} (\overline{\phi_j} - \phi_j^*), \end{aligned} \tag{11}$$

where $K_{nj} = -\sum_l \alpha_{nl} (\overline{\partial^2 S/\partial \phi_l \, \partial \phi_j})^*$ (Reif 1965). For larger departures, coefficients K_{nj} presumably become dependent upon state ϕ_j. Lacking further information at larger $\overline{\phi_j}-\phi_j^*$, we presume K_{nj} to be independent of $\overline{\phi_j}$ and moreover suppose diagonal dominance, so that $\mathrm{d}\overline{\phi_n}/\mathrm{d}t \approx K_n(\overline{\phi_n}-\phi_n^*)$.

For flows having sufficiently weak forcing and dissipation, nonlinear interactions remain the dominant dynamical influence. We anticipate that the entropy maximization tendency will lead to behaviour like (11), though a rigorous basis for such an assumption is lacking. Working from this conjecture, Holloway (1992) suggested that the effects of topographic stress due to unresolved eddies can be accounted for through a term

$$A_m \nabla^m (\boldsymbol{u} - \boldsymbol{u}^*), \tag{12}$$

replacing the usual eddy viscosity operating on the horizontal velocity $\boldsymbol{u}$. Here m is an even integer, while $\boldsymbol{u}^*$ represents the equilibrium flow specified by streamfunction (5). In practice, $\boldsymbol{u}^*$ has been determined from the limit of (5) on scales coarser than $\mu^{-1/2}$, so that

$$\psi^* = \lambda^2 h, \tag{13}$$

where we identify λ with $\mu^{-1/2}$. Because prior knowledge of μ is imprecise, modelling efforts employing (12) and (13) have treated λ as an adjustable parameter. We have used λ rather than μ in (13) to recognize that the chosen λ may differ from the unknown $\mu^{-1/2}$. In principle, one could determine ψ^* from the relation $\mu\psi^* = q^* = \nabla^2\psi^* + h$ which describes inviscid equilibrium flow exactly, instead of from (13). This may be preferable in instances where scales finer than $\mu^{-1/2}$ are resolved.

3.1. *Restoring tendency for inviscid flows*

To assess the applicability of these ideas, we first evaluate elements of $\boldsymbol{K}$ for inviscid barotropic models I1 and I2 having similar E and Q to models R1 and R2. (The model pairs also are characterized by similar μ: 19.6 for R1 *vs.* 16.8 for I1, and 294 for R2 *vs.* 284 for I2, in units of k_0^2.) This illustrates statistical mechanical ideas in a context where they are rigorously founded. Later, we evaluate $\boldsymbol{K}$ for forced–dissipative models R1 and R2.

For system parameters ϕ_n we adopt the ensemble-mean modal amplitudes $\bar{\zeta}_k$. Consider what happens when a steady torque $\bar{F}$, identical for each member of the ensemble, is applied to mode $\boldsymbol{k}_f$. (For $\bar{F}(x, y)$ to be real, a torque $\bar{F}^\dagger$ must simultaneously be applied to mode $-\boldsymbol{k}_f$.) Although the torque tends to modify E and Q, these quantities can be held constant by continuously tuning the coefficients ν_0 and ν_4

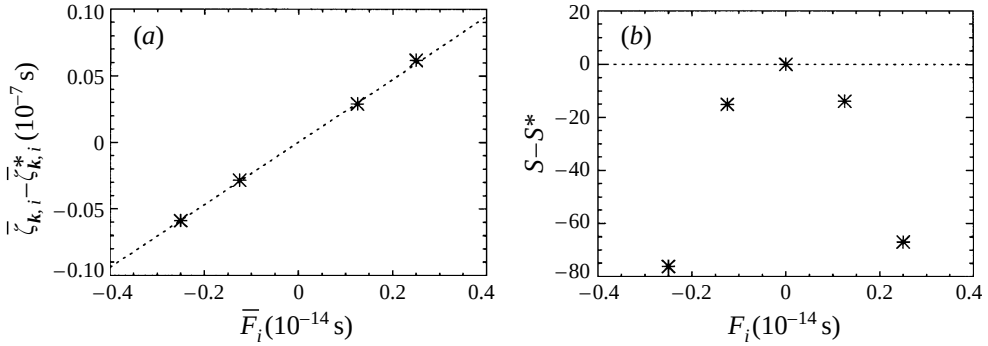

FIGURE 4. (*a*) Measured displacement of mean mode amplitude $\bar{\zeta}_{k,i}-\bar{\zeta}^*_{k,i}$ *vs.* amplitude $\bar{F}_i$ of steady applied torque, for particular $(\boldsymbol{k}, i)$ with $k = 5$. Dotted line: mean slope implied by the four measurements. (*b*) Entropy of the modified equilibria, minus entropy S^* of the absolute equilibrium at $\bar{F}_i = 0$.

in the dissipation operator (8), as described in the Appendix. The imposed forcing and dissipation also affect the equilibrium spectra. We take care that forcing and dissipation are sufficiently weak that departures from equilibrium are slight. This has been verified by comparing perturbed and unperturbed energy spectra.

The model is run until a modified statistical equilibrium is achieved, and temporal-mean $\bar{\zeta}_{\boldsymbol{k}}$ are computed. On the basis of (11), we expect the restoring tendency to balance the applied torque and dissipation. Using the subscript $i = 1, 2$ to denote real and imaginary parts, we have

$$\frac{\partial\bar{\zeta}_{\boldsymbol{k},i}}{\mathrm{d}t} \approx \bar{F}_i\,\delta_{\boldsymbol{k},\boldsymbol{k}_f} + (-1)^{i-1}\bar{F}_i\,\delta_{\boldsymbol{k},-\boldsymbol{k}_f} + \bar{D}_{\boldsymbol{k},i} - \sum_{\boldsymbol{k}'}\sum_{i'} K_{\boldsymbol{k},\boldsymbol{k}',i,i'}(\bar{\zeta}-\bar{\zeta}^*)_{\boldsymbol{k}',i'} = 0, \tag{14}$$

where $\bar{\zeta}^*_{\boldsymbol{k}}$ is the inviscid equilibrium mean vorticity implied by (5), and δ is the Kroneker delta. Because forcing is concentrated at $\pm\boldsymbol{k}_f$, whereas dissipation is broadband, $\bar{D}_{\boldsymbol{k}_f,i} \ll \bar{F}_i$, so that the primary balance at $\boldsymbol{k}_f$ is between $\bar{F}$ and the restoring terms. For simplicity, we suppose that the diagonal elements of $\boldsymbol{K}$, henceforth denoted $K_{\boldsymbol{k},i}$, dominate. (In the following examples, $|\bar{\zeta}_{\boldsymbol{k}_f}-\bar{\zeta}^*_{\boldsymbol{k}_f}|$ typically is two to three times the next largest $|\bar{\zeta}_{\boldsymbol{k}}-\bar{\zeta}^*_{\boldsymbol{k}}|$.) The $K_{\boldsymbol{k},i}$ can then be found from

$$K_{\boldsymbol{k},i} \approx \frac{\bar{F}_i}{\bar{\zeta}_{\boldsymbol{k},i}-\bar{\zeta}^*_{\boldsymbol{k},i}}, \tag{15}$$

evaluated at $\boldsymbol{k} = \boldsymbol{k}_f$. We considered two to four values of $\bar{F}_i$ for numerous choices of $(\boldsymbol{k}_f, i)$, and estimated $K_{\boldsymbol{k},i}$ from averages of the values implied by (15). To assess the generality of this procedure, we repeated some of the measurements, this time maintaining E and Q by tuning the coefficients of the alternative dissipation law $D_{\boldsymbol{k}} = (\nu_0 + \nu_2 k^2)\,\zeta_{\boldsymbol{k}}$. The $K_{\boldsymbol{k},i}$ determined by the two procedures differed by less than 1 %.

Figure 4(*a*) shows how $\bar{\zeta}_{\boldsymbol{k}_f,i}-\bar{\zeta}^*_{\boldsymbol{k}_f,i}$ varies with $\bar{F}_i$ for a mode having $k = 5$. Entropy $S = \frac{1}{2}\sum_{\boldsymbol{k}} \ln\{|\zeta_{\boldsymbol{k}}|^2|h_{\boldsymbol{k}}|^2 - |\zeta_{\boldsymbol{k}}\,h^{\dagger}_{\boldsymbol{k}}|^2\}$, computed by the shell-averaging method of Zou & Holloway (1994), is shown for each measurement in figure 4(*b*). The results are consistent with the linear force–response relationship (15) and with the quadratic behaviour (11) of the entropy.

Figure 5(*a*, *b*) shows measured $K_{\boldsymbol{k},i}$ for numerous choices of $(\boldsymbol{k}, i)$ for models I1 and I2. In both cases, the restoring coefficients increase with k at large k. The restoring

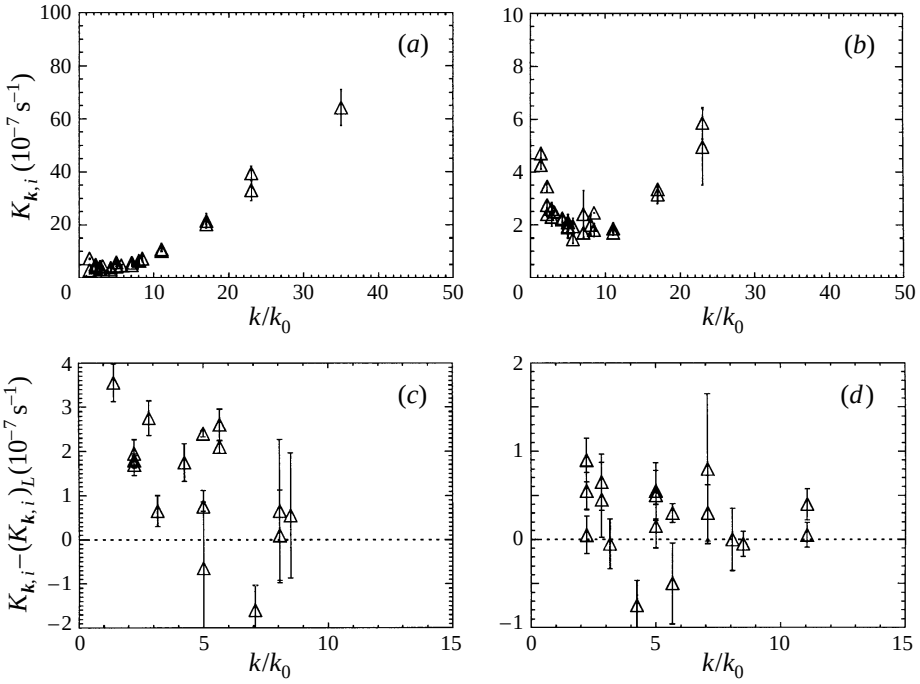

FIGURE 5. (*a*) Restoring coefficients $K_{k,i}$ *vs.* k for inviscid high-resolution model I1 having similar E and Q to model R1. (*b*) As (*a*), but for I2, the inviscid counterpart to R2. (*c*) The difference in restoring coefficients between model I1 and a version of I1 truncated at $k_L = 10$. (*d*) The difference in restoring coefficients between I2 and a version if I2 truncated at $k_L = 21$. The error bars indicate standard deviations.

coefficients exhibit minima at $k \approx 3$ in I1, and at $k \approx 10$ in I2. Why the coefficients should vary in this manner has not been determined. The coefficients were recomputed for low-resolution versions of I1 and I2, truncated at wavenumbers $k_L \ll k_1$. Figure 5(*c*, *d*) shows the differences $K_{k,i}-(K_{k,i})_L$, where $(K_{k,i})_L$ are the restoring coefficients for the low-resolution models. It is this difference, reflecting the restoring tendency due to unresolved scales, that the topographic stress parameterization (12) and (13) represents. The measured $K_{k,i}-(K_{k,i})_L$ exhibit significant scatter, but no obvious systematic variation with k. This suggests the use of $m = 0$ in (12).

3.2. *Restoring tendency for forced–dissipative flows*

The statistical mechanical principles cited above are premised on exact conservation of E and Q. Hence, they cannot rigorously be applied to the forced–dissipative models R1 and R2. However, because $t_e \ll t_\nu$ for these models, nonlinear interactions dominate the dynamics, and a restoring tendency qualitatively similar to that of inviscid systems can be expected.

We evaluate the restoring coefficients $K_{k,i}$ for models R1 and R2 by a procedure similar to the one described above. The primary difference is that no effort is made to fix E and Q, which normally fluctuate in these forced–dissipative models. Applying a steady torque $\bar{F}_{k,i}$ thus alters the mean values $\bar{E}$ and $\bar{Q}$. However, because there is dissipation these changes are slight for sufficiently small $\bar{F}_{k,i}$.

Restoring coefficients $K_{k,i}$ for models R1 and R2 are shown in figure 6. The coefficients vary with k in much the same way as for models I1 and I2, but are generally

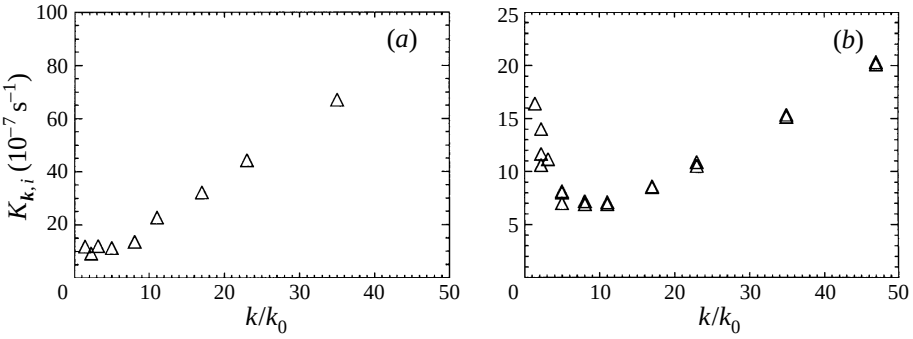

FIGURE 6. Restoring coefficients $K_{k,i}$ for forced–dissipative high-resolution models (*a*) R1 and (*b*) R2. Standard deviations are small compared to the size of the symbols.

larger. That K_k differs between the forced–dissipative and inviscid models is not surprising. Although the pairs R1/I1 and R2/I2 exhibit similar mean flows, their eddy properties differ. Figures 5 and 6 demonstrate that the restoring tendency in forced–dissipative flows is qualitatively similar to that in inviscid flows.

For inviscid models, we showed that the restoring tendency weakens with decreasing resolution. This cannot be shown directly for forced–dissipative models, because truncation at $k_L \ll k_1$ leads to changes in $\bar{\zeta}_k$ unless some subgrid-scale parameterization prevents this. Whether $K_{k,i}$ changes because of diminished resolution or changes in the flow structure thus becomes unclear. However, the restoring tendency for inviscid and forced–dissipative models is demonstrably similar at high resolution. We infer that eliminating small-scale eddies weakens $K_{k,i}$ for forced–dissipative flows in much the same way as for inviscid ones.

4. Topographic stress and dissipation of Q

In §3, we considered the ability of the topographic stress parameterization to represent unresolved forcing by topographic stress. Here we examine the implications of the parameterization for dissipation of energy and potential enstrophy. Suppose the cutoff wavenumber k_1 is so large that further increasing k_1 has no appreciable effect, as for models R1 and R2. We refer to this as 'model R'. Consider also a low-resolution counterpart with spectral cutoff $k_L \ll k_1$, together with some parameterization to represent the unresolved scales. This we call 'model L'.

4.1. *Eddy viscosity parameterization*

Consider E- and Q-dissipation in model R. Assume that F is confined to the large scales $k \leqslant k_L$ resolved by model L, and is temporally random, being determined by (9). We suppose also that F has zero ensemble mean, where the ensemble includes different realizations of the random process $G_k(t)$. Dissipation is given by $D = -\nu_k \zeta_k$, where ν_k is a positive scale-dependent viscosity as in (8). Multiplying (1) by $k^{-2}\zeta_k^\dagger$, where the dagger denotes complex conjugation, summing over $\boldsymbol{k}$, and ensemble averaging yields

$$\frac{\partial \bar{E}}{\partial t} = \sum_{k=k_0}^{k_1} \mathscr{R}\{\overline{F_k \zeta_k^\dagger} k^{-2}\} - \sum_{k=k_0}^{k_1} \nu_k \bar{E}_k = 0 \tag{16}$$

for model R in statistical equilibrium, where $\bar{E}_k = \overline{|\zeta_k|^2}/k^2$ and $\zeta_k' = \zeta_k - \bar{\zeta}_k$. (In the first

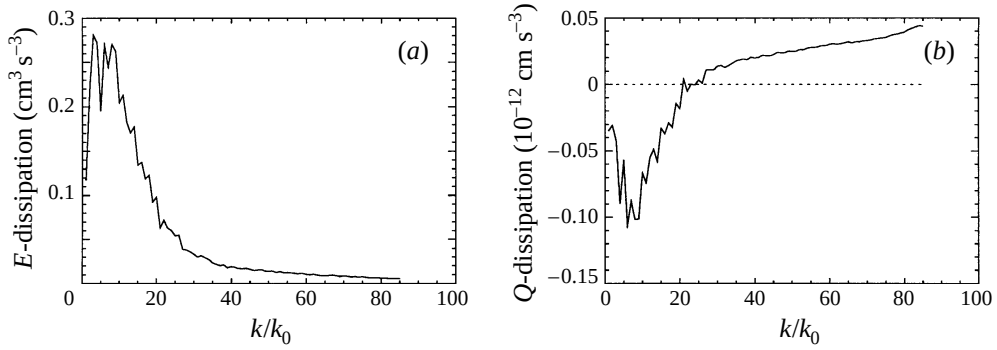

FIGURE 7. Rates of (*a*) energy and (*b*) potential enstrophy dissipation as functions of k, for high-resolution model R2.

sum, we have used the fact that $\overline{F_k \bar{\zeta}_k^\dagger} = 0$ for temporally random F_k.) Figure 7(*a*) shows energy dissipation as a function of wavenumber for model R2.

Now initialize model L with a truncated solution of model R. For model L to replicate the resolved scales of model R, its ensemble-mean properties must retain their initial values. To keep $\bar{E}$ the same, we can make up for discarded E-dissipation at $k > k_L$ by increasing viscosity to $\tilde{\nu}_k > \nu_k$, such that

$$\frac{\partial \bar{E}}{\partial t} = \sum_{k=k_0}^{k_L} \mathscr{R}\{\overline{F_k \zeta_k'^\dagger} k^{-2}\} - \sum_{k=k_0}^{k_L} \tilde{\nu}_k \bar{E}_k = 0 \tag{17}$$

For model L. This constitutes an eddy viscosity parameterization.

Next evaluate Q-dissipation in model R. Multiplying equation (1) by $q_k^\dagger = \zeta_k^\dagger + h_k^\dagger$, summing, and averaging yields

$$\begin{aligned}\frac{\partial \bar{Q}}{\partial t} &= \sum_{k=k_0}^{k_1} \mathscr{R}\{\overline{F_k \zeta_k'^\dagger}\} - \sum_{k=k_0}^{k_1} \nu_k(\overline{|\zeta_k'|^2} + \mathscr{R}\{\overline{\zeta_k h_k^\dagger}\}) \\ &= \sum_{k=k_0}^{k_1} \mathscr{R}\{\overline{F_k \zeta_k'^\dagger}\} - \sum_{k=k_0}^{k_1} \nu_k(\overline{|\zeta_k'|^2} + |\bar{\zeta}_k|^2 + \mathscr{R}\{\bar{\zeta}^k h_k^\dagger\}).\end{aligned} \tag{18}$$

Guided by §2.3, we suppose that for temporally random F the mean flow is approximated by (5), so that

$$\bar{\zeta}_k = \frac{-k^2 h_k}{\mu + k^2} \tag{19}$$

and

$$|\bar{\zeta}_k|^2 + \mathscr{R}\{\bar{\zeta}_k h_k^\dagger\} = \frac{-\mu k^2 |h_k|^2}{(\mu + k^2)^2}. \tag{20}$$

Using $E_k^{(f)} = k^{-2}\overline{|\zeta_k'|^2}$ and $E_k^{(m)} = k^{-2}|\bar{\zeta}^2| = k^2|h_k|^2/(\mu + k^2)^2$, (18) becomes

$$\frac{\partial \bar{Q}}{\partial t} = \sum_{k=k_0}^{k_1} \mathscr{R}\{\overline{F_k \zeta_k'^\dagger}\} - \sum_{k=k_0}^{k_1} [\nu_k k^2 E_k^{(f)} - \mu E_k^{(m)}] = 0. \tag{21}$$

Whereas E-dissipation is positive definite, Q-dissipation can become negative at small k, as seen in figure 7(*b*). Equation (21) indicates that this is a general result, provided

the steady component of the flow is sufficiently energetic, and $E_k^{(f)}/E_k^{(m)}$ does not decrease more rapidly with k than k^{-2}. (Intuitively, we expect the smallest-scale flows to be unsteady, and the latter condition to be satisfied. For example, $E_k^{(f)}/E_k^{(m)} \approx$ constant in models R1 and R2, as seen in figure 3.) The negative Q-dissipation is associated with the steady topographically correlated part of the flow. Because $\bar{\zeta}$ is anticorrelated with h, viscous decay of $\bar{\zeta}$ leads to increasing $Q^{(m)} = \int\int |\bar{\zeta}+h|^2 \,\mathrm{d}x\,\mathrm{d}y$.

If k_L in a coarse-resolution model is sufficiently small that net dissipation of Q is negative, the usual procedure of accounting for subgrid-scale dissipation by enhancing viscosity cannot possibly yield the desired $\bar{Q}$. Increased viscosity increases Q, making the problem worse!

4.2. *Topographic stress parameterization*

When applied to (1), the topographic stress parameterization (12) and (13) becomes $A_m \nabla^m(\zeta_k - \zeta_k^*)$, with $\zeta_k^* = -k^2\lambda^2 h_k$. Then†

$$\frac{\partial \bar{E}}{\partial t} = \sum_{k=k_0}^{k_L} \mathscr{R}\{\overline{F_k' \zeta_k'^{\dagger}}\, k^{-2}\} - \sum_{k=k_0}^{k_L} A_m k^m [E_k^{(f)} + [1-\lambda^2(\mu+k^2)]\, E_k^{(m)}] \tag{22}$$

and

$$\frac{\partial \bar{Q}}{\partial t} = \sum_{k=k_0}^{k_L} \mathscr{R}\{\overline{F_k' \zeta_k'^{\dagger}}\} - \sum_{k=k_0}^{k_L} A_m k^m [k^2 E_k^{(f)} - \mu[1-\lambda^2(\mu+k^2)]\, E_k^{(m)}]. \tag{23}$$

The topographic stress term offsets generation of Q by large-scale mean flow, and guarantees positive net dissipation of Q for λ sufficiently large. The topographic stress term thus can prevent $\bar{Q}$ from increasing, whereas simply enhancing viscosity cannot.

Optimal values for A_m and λ can be estimated by equating the E-dissipation terms in (16) with those (22), and the Q-dissipation terms in (21) with those in (23). This yields

$$A_m = \sum_{k=k_0}^{k_1} \nu_k(\mu_R + k^2)\,[E_k^{(f)}]_R \Big/ \sum_{k=k_0}^{k_L} k^m(\mu_L + k^2)\,[E_k^{(f)}]_L, \tag{24}$$

and

$$\lambda^2 = \sum_{k=k_0}^{k_L} A_m k^m [\bar{E}_k]_L - \sum_{k=k_0}^{k_1} \nu_k [\bar{E}_k]_R \Big/ \sum_{k=k_0}^{k_L} A_m k^m (\mu_L + k^2)\,[E_k^{(m)}]_L, \tag{25}$$

where the subscripts R and L denote properties of models R and L. Equation (24) shows that A_m scales with ν_k, the viscosity in model R, and is governed by the fluctuating part of the flow.

5. Performance of the parameterization

In this section, the topographic stress parameterization is implemented in low-resolution models. Alternatives are considered, and results are compared to high-resolution models.

For models R1 and R2 having truncation wavenumber $k_1 = 85$, we consider low-resolution counterparts truncated at $k_L = 10$ and $k_L = 5$. The comparisons involving model R1 we call the 'high-E' case, and those involving R2 the 'low-E' case. Initial

† Here the topographic stress term (12) replaces the entire viscous operator as in Eby & Holloway (1994). In the low-resolution models of §5, we replace only the biharmonic friction term, while retaining bottom friction.

	High E		Low E	
Parameter	$k_L = 10$	$k_L = 5$	$k_L = 10$	$k_L = 5$
Eddy:				
ν_4 (cm^4 s^{-1})	3.1×10^{18}	3.1×10^{20}	4.5×10^{18}	6.5×10^{20}
Topo. $m = 0$:				
A_0 (s^{-1})	1.5×10^{-7}	4.0×10^{-7}	2.5×10^{-7}	5.0×10^{-7}
λ (km)	33.4	40.5	12.3	12.3
Topo. $m = 2$:				
A_2 (cm^2 s^{-1})	2.1×10^6	1.3×10^7	3.8×10^6	2.5×10^7
λ (km)	26.3	37.1	11.4	11.9

TABLE 3. Optimal parameter values for low-resolution models

conditions consist of instantaneous solutions of the high-resolution models, truncated at k_L. The topographic stress term replaces the biharmonic friction term in (8), and bottom friction ν_0 is left unchanged. We consider $m = 0$ and $m = 2$, tuning topographic stress parameters A_m and λ to match $\bar{E}$ and $\bar{Q}$ of the high-resolution model on the mutually resolved scales. Best-fit parameters are listed in table 3.

Similar fitting exercises were attempted with eddy viscosity formulations. We first treated both coefficients in the dissipation law $\nu_0 + \nu_4 k^4$ as parameters. However, these behaved badly, ν_0 reversing sign even when $k_L > \mu^{1/2}$, and both parameters becoming singular and changing sign when $k_L \sim \mu^{1/2}$. We then considered dissipation $\nu_0 + \nu_2 k^2 + \nu_4 k^4$, leaving ν_0 at its high-resolution model value, and treating ν_2 and ν_4 as parameters. When $k_L > \mu^{1/2}$, ν_2 is consistently negative, and the dissipation law resembles that obtained by Leith (1971) for two-dimensional turbulence. However, when $k_L \sim \mu^{1/2}$ the parameters again become singular and change sign. Next we reconsidered dissipation $\nu_0 + \nu_4 k^4$, augmenting Q-dissipation by the anticipated potential vorticity (APV) method. The APV method dissipates Q while conserving E through a term

$$\frac{\theta}{k_L^{2\alpha}} J[\psi, \nabla^{2\alpha}(\psi, q)], \tag{26}$$

where θ is a parameter and α a non-negative integer (Sadourny & Basdevant 1985; Vallis & Hua 1988). Target $\bar{E}$ was matched by tuning ν_4. We considered $\alpha = 0$, 2 and 4, and varied θ, attempting to bring $\bar{Q}$ to its target value. However, we were unable to attain target $\bar{Q}$ before θ was chosen so large that the model became unstable. Because we could not achieve a stable model with target $\bar{E}$ and $\bar{Q}$ using any of these methods, we settled upon comparing the topographic stress models to more conventional eddy viscosity models, in which ν_0 is left at its high-resolution model value, and ν_4 is tuned to match target $\bar{E}$.

To assess the skill, we considered how accurately low-resolution models represent the strength and form of the mean flows. Results are summarized in table 4. The strength of the steady component is measured by the ratio $E^{(m)}/\bar{E}$ of mean-flow energy to mean total energy. The mean flow is much too feeble in the eddy viscosity models, especially for small k_L, and $\bar{Q}$ is too large. Evidently, these models are unable to dissipate Q effectively, due to truncation of the fine scales that dominate Q-dissipation. Increased $\bar{Q}$ is accompanied by weakened mean flow, as well as increased $\mu = \bar{q}/\bar{\psi}$, which from (5) distorts the mean streamlines. By contrast, these properties are better represented by the topographic stress models.

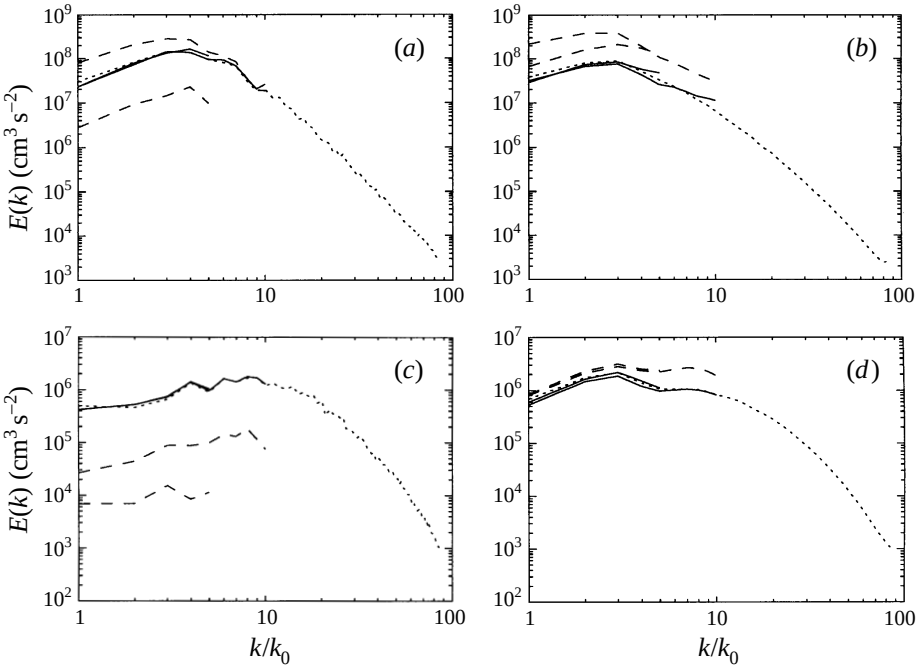

FIGURE 8. Mean and fluctuating energy spectra $E^{(m)}$ and $E^{(f)}$: (*a*) $E^{(m)}$, high E; (*b*) $E^{(f)}$, high E; (*c*) $E^{(m)}$, low E; (*d*) $E^{(f)}$, low E. Dotted lines: high-resolution models. Dashed lines: Eddy viscosity models for $k_L = 10$ and $k_L = 5$. Solid lines: topographic stress models for $k_L = 10$ and $k_L = 5$, with $m = 0$.

	$k_L = 85$	$k_L = 10$				$k_L = 5$			
				Topo.				Topo.	
	High	High	Eddy	$m = 0$	$m = 2$	High	Eddy	$m = 0$	$m = 2$
High E:									
$\bar{E}$ (cm^2 s^{-3})	57.1	52.4	52.4	51.7	51.9	38.3	38.4	38.5	38.4
$\bar{Q}$ (10^{-12} s^{-2})	5.92	4.82	6.61	4.72	4.76	4.00	6.59	3.89	3.89
$E^{(m)}/E$	0.666	0.661	0.432	0.688	0.652	0.624	0.073	0.636	0.623
μ	19.6	19.6	29.0	19.0	19.1	19.6	69.0	20.3	20.5
$\bar{\Delta}$	—	—	0.103	0.070	0.076	—	0.523	0.103	0.117
Low E:									
$\bar{E}$ (cm^2 s^{-2})	2.18	1.15	1.16	1.14	1.15	0.53	0.54	0.53	0.53
$\bar{Q}$ (10^{-12} s^{-2})	9.44	8.46	9.12	8.41	8.41	6.95	7.28	6.84	6.96
$E^{(m)}/\bar{E}$	0.563	0.490	0.043	0.523	0.520	0.355	0.0023	0.371	0.377
μ	294	294	1112	308	312	294	2319	311	323
$\bar{\Delta}$	—	—	0.585	0.055	0.054	—	0.866	0.051	0.055

TABLE 4. Comparison of high-resolution model and best low-resolution model results. 'High' denotes high-resolution models, truncated at the wavenumbers indicated. 'Eddy' denotes low-resolution models with eddy viscosity parameterization. 'Topo.' denotes low-resolution models with topographical stress parameterization, for $m = 0$ and $m = 2$. The ratio μ is expressed in units of k_0^2.

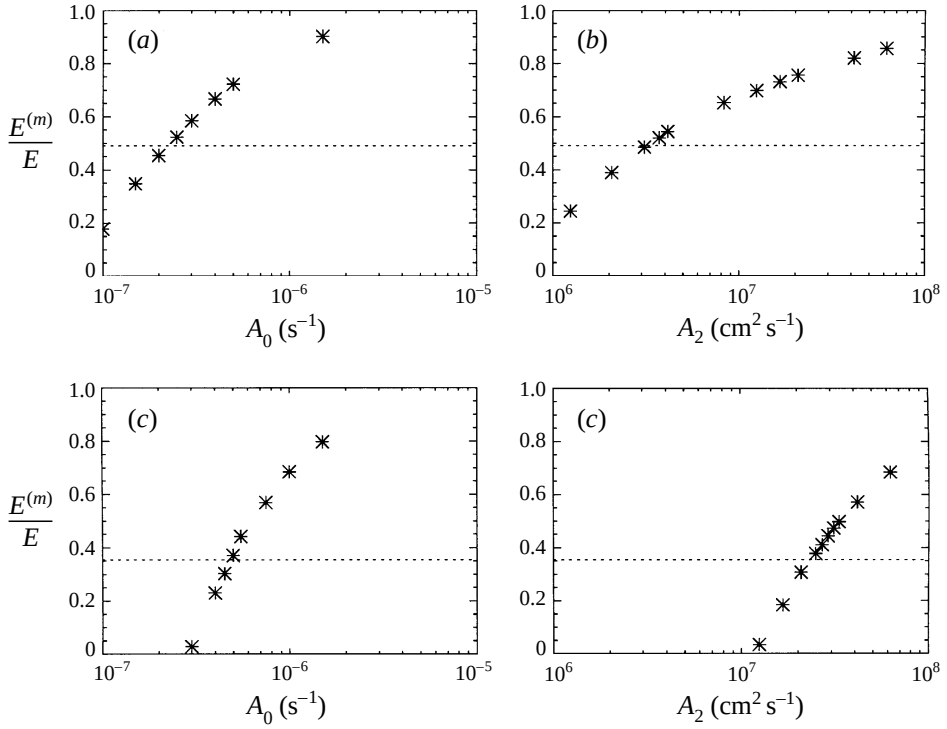

FIGURE 9. $E^{(m)}/E$ for low-E topographic stress models, as restoring coefficients A_m are varied: (*a*) $m = 0$, $k_L = 10$; (*b*) $m = 2$, $k_L = 10$; (*c*) $m = 0$, $k_L = 5$; (*d*) $m = 2$, $k_L = 5$. Dotted lines indicate $E^{(m)}/\bar{E}$ for $K \leqslant k_L$ in high-resolution models.

A measure of the skill of low-resolution models in representing mean flow is

$$\bar{\Delta} = \iint (\bar{\psi}_L - \bar{\psi}_R)^2 \,\mathrm{d}x\,\mathrm{d}y \Big/ \iint \bar{\psi}_R^2 \,\mathrm{d}x\,\mathrm{d}y, \tag{27}$$

where $\bar{\psi}_L$ is the mean streamfunction of the low-resolution model, and $\bar{\psi}_R$ is that of the high-resolution model for wavenumbers $k \leqslant k_L$. Smaller $\bar{\Delta}$ indicates better model performance. For the topographic stress models, $\bar{\Delta} \lesssim 0.1$ in all cases, whereas $\bar{\Delta} \sim O(1)$ for the lowest-resolution eddy viscosity models. The eddy viscosity models fare particularly badly when the lengthscale $\mu^{-1/2}$ is poorly resolved.

The mean and fluctuating energy spectra for the high- and low-resolution models are compared in figure 8. Again, the low-resolution topographic stress models (solid lines) adequately reproduce the high-resolution model results. By comparison, the eddy viscosity models (dashed lines) perform poorly, exhibiting too much energy in the fluctuating component at the expense of the mean component, particularly as k_L decreases.

We next consider the sensitivity of the topographic stress models to A_m. For each A_m, λ is chosen to match target $\bar{E}$ (whereas $\bar{Q}$ may differ from its target value.) Figure 9 shows how $E^{(m)}/\bar{E}$ varies with A_0 and A_2. Dotted lines indicate properties of high-resolution models. The fidelity of the topographic stress models becomes more sensitive to A_m as k_L decreases.

Figure 10 compares the best-fit A_m and λ with optimal values predicted from the procedure in §4.2, indicated by curves. Reasonable agreement is seen.

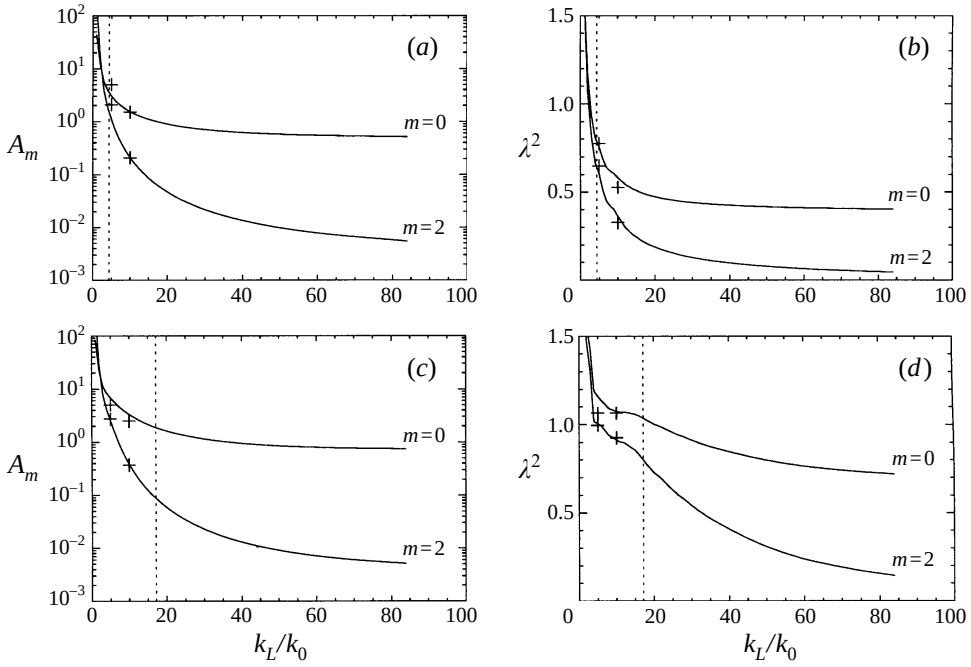

FIGURE 10. Comparison of optimal topographic stress parameters from models (+) and prediction via procedure in §4.2 (——), for $m = 0$ and $m = 2$. (*a*) High E, A_m; (*b*) high E, λ^2; (*c*) low E, A_m; (*d*) low E, λ^2. A_0 is in units of 10^{-7} s^{-1}, and A_2 is in units of 10^7 cm^2 s^{-1}; λ^2 is in units of μ^{-1}. The dotted lines indicate $k_L = \mu^{1/2}$.

6. Choice of parameters

For the subgrid-scale parameterization described by equations (12) and (13) to be useful, practical means are needed for assigning parameters m, A_m and λ.

6.1. *Choice of m and A_m*

In §3.1 we found that for inviscid models I1 and I2, the reduction $K_k - (K_k)_L$ of the restoring coefficient at coarse resolution shows no clear trend with k. This motivated the choice $m = 0$ in §5, although this choice was not markedly superior to $m = 2$. In modelling practice, both $m = 0$ and $m = 2$ have been used without dramatic difference between the two forms (M. Eby, private communication).

Because model results are not strongly dependent on m, it is not surprising that the choice of A_m is not tightly constrained. Like eddy viscosity, A_m increases with decreasing (i.e. coarser) resolution, as seen in figure 10. In modelling practice, it is usual to set eddy viscosity as small as possible without admitting overly noisy fields. An exciting possibility, which remains to be explored, is that with the topographic stress parameterization it will be practical to assign relatively large values to A_m. This may make models less prone to numerical instability, while improving model fidelity.

6.2. *Choice of λ*

For the high-E and low-E cases above, the optimal λ^2 is within about 10% of μ^{-1} when $k_L < \mu^{1/2}$ (figure 10). This is in accord with the identification $\lambda^2 \equiv \mu^{-1}$ made in formulating the parameterization (12) and (13). For the oceans and even for the barotropic models considered here, there are no clear rules for determining μ from observable quantities such as mean energy and topographic variance. We remark that in the high-resolution models R1 and R2, the wavenumber $\mu^{-1/2}$ lies roughly where the

fluctuating energy spectrum begins to drop off rapidly with k (figure 3). In the oceans, eddy spectra fall off rapidly on scales shorter than the first radius of deformation. Crudely, this idea was used by Eby & Holloway (1994), who took λ to be a weak function of latitude ranging from 12 km near the equator to 3 km at the poles. We caution, however, that a simple scaling by local deformation radius would be hazardous: λ is a statistical property much like temperature, and may be expected to 'thermalize' over distances larger than characterize variations in deformation radius. Improving *a priori* estimation of λ for practical modelling exercises looms as an important research goal.

7. Conclusions

The properties of a proposed parameterization of unresolved topographic stress were examined in simple barotropic models. The parameterization was shown to represent contribution of unresolved eddies to the tendency for entropy maximization, and to dissipation of potential enstrophy, offsetting potential enstrophy generation on larger scales due to viscous decay of topographically correlated mean currents. Low-resolution models employing the topographic stress parameterization reproduced by behaviour of high-resolution models on the larger scales, whereas models using eddy viscosity parameterizations did not.

This study represents an initial effort to establish a basis for topographic stress parameterization in ocean models. More investigations will be needed to account for properties not considered here, including stratification, mean forcing, and finite-amplitude topography. The persistence of the mean-flow tendency in high-resolution models that incorporate these effects motives further work.

This work was supported by the Office of Naval Research (N00014-92-J-1775).

Appendix. Adjusting dissipation to conserve E and Q

In §3.1, we measure restoring coefficients K_k for inviscid flows by applying weak steady torques $\bar{F}_k$. To maintain conservation of E and Q, we adjust the coefficients of a compensating dissipation $\nu_0+\nu_4 k^4$.

Conservation of E and Q implies

$$\frac{\partial E}{\partial t} = 0 = \sum_{k=k_0}^{k_1} \bar{F}_k \zeta_k^\dagger k^{-2} - \nu_0 \sum_{k=k_0}^{k_1} |\zeta_k|^2 k^{-2} - \nu_4 \sum_{k=k_0}^{k_1} |\zeta_k|^2 k^2, \tag{A 1}$$

$$\frac{\partial Q}{\partial t} = 0 = \sum_{k=k_0}^{k_1} \bar{F}_k (\zeta_k^\dagger + h_k^\dagger) - \nu_0 \sum_{k=k_0}^{k_1} (|\zeta_k|^2 + \zeta_k h_k^\dagger) - \nu_4 \sum_{k=k_0}^{k_1} (|\zeta_k|^2 + \zeta_k h_k^\dagger) k^4. \tag{A 2}$$

Solving for ν_0, ν_4 yields

$$\nu_0 = (E_F Q_4 - E_4 Q_F)/(E_0 Q_4 - E_4 Q_0), \tag{A 3}$$

$$\nu_4 = (E_0 Q_F - E_F Q_0)/(E_0 Q_4 - E_4 Q_0), \tag{A 4}$$

where

$$E_0 = \sum_{k=k_0}^{k_1} |\zeta_k|^2 k^{-2}, \quad E_4 = \sum_{k=k_0}^{k_1} |\zeta_k|^2 k^2, \quad E_F = \sum_{k=k_0}^{k_1} \bar{F}_k \zeta_k^\dagger k^{-2}, \tag{A 5 a–c}$$

$$Q_0 = \sum_{k=k_0}^{k_1} (|\zeta_k|^2 + \zeta_k h_k^\dagger), \quad Q_4 = \sum_{k=k_0}^{k_1} (|\zeta_k|^2 + \zeta_k h_k^\dagger) k^4, \quad Q_F = \sum_{k=k_0}^{k_1} \bar{F}_k (\zeta_k^\dagger + h_k^\dagger). \tag{A 6 a–c}$$

If $\bar{F}_k$ is applied to one mode at a time, as in §2, the sums in (A 5 c) and (A 6 c) reduce to a single term.

REFERENCES

Alvarez, A., Tintore, J., Holloway, G., Eby, M. & Beckers, J. M. 1994 Effect of topographic stress on the circulation in the western Mediterranean. *J. Geophys. Res.* **99**, 16053–16064.

Bretherton, F. P. & Haidvogel, D. B. 1976 Two-dimensional turbulence above topography. *J. Fluid Mech.* **78**, 129–154.

Canuto, C., Hussaini, M. Y., Quarteroni, A. & Zang, T. A. 1988 *Spectral Methods in Fluid Mechanics*. Springer.

Carnevale, G. F. 1982 Statistical features of the evolution of two-dimensional turbulence. *J. Fluid Mech.* **122**, 143–153.

Carnevale, G. F. & Frederiksen, J. S. 1987 Nonlinear stability and statistical mechanics of flow over topography. *J. Fluid Mech.* **175**, 157–181.

Eby, M. & Holloway, G. 1994 Sensitivity of a large-scale ocean model to a parameterization of topographic stress. *J. Phys. Oceanogr.* **24**, 2577–2588.

Fyfe, J. & Marinone, G. 1995 On the role of unresolved eddies in a model of the residual currents in the central Strait of Georgia, B.C. *Atmos.-Ocean* **33**, 613–619.

Gazdag, J. 1976 Partially-corrected Adams-Bashforth schemes. *J. Comput. Phys.* **20**, 196–207.

Griffa, A., Chassignet, E. P., Coles, V. & Olson, D. B. 1996 Inertial gyre solutions from a positive equation ocean model. *J. Mar. Res.* **54**, 653–677.

Haidvogel, D. B. & Brink, K. H. 1986 Mean currents driven by topographic drag over the continental shelf and slope. *J. Phys. Oceanogr.* **16**, 2159–2171.

Holloway, G. 1987 Systematic forcing of large-scale geophysical flows by eddy-typography interaction. *J. Fluid Mech.* **184**, 463–476.

Holloway, G. 1992 Representing topographic stress for large-scale ocean models. *J. Phys. Oceanogr.* **22**, 1033–1046.

Holloway, G. & Sou, T. 1996 Measuring the skill of a topographic stress parameterization in a large-scale ocean model. *J. Phys. Oceanogr.* **26**, 1088–1092.

Holloway, G., Sou, T. & Eby, M. 1995 Dynamics of circulation of the Japan Sea. *J. Mar. Res.* **53**, 539–569.

Leith, C. E. 1971 Atmospheric predictability and two-dimensional turbulence. *J. Atmos. Sci.* **28**, 145–161.

Miller, J. 1990 Statistical mechanics of Euler equations in two dimensions. *Phys. Rev. Lett.* **22**, 2137–2140.

Reif, F. 1965 *Fundamentals of Statistical and Thermal Physics*, §15.18. McGraw Hill.

Robert, R. & Sommeria, J. 1991 Statistical equilibrium states for two-dimensional flows. *J. Fluid Mech.* **229**, 291–310.

Sadourney, R. & Basdevant, C. 1985 Parameterization of subgrid scale barotropic and baroclinic eddies in quasigeostrophic models: anticipated potential vorticity method. *J. Atmos. Sci.* **42**, 1353–1363.

Salmon, R., Holloway, G. & Hendershott, M. C. 1976 The equilibrium statistical mechanics of simple quasi-geostrophic models. *J. Fluid Mech.* **75**, 691–703.

Sommeria, J., Staquet, C. & Robert, R. 1991 Final equilibrium state of a two-dimensional shear layer. *J. Fluid Mech.* **233**, 661–689.

Sou, T., Holloway, G. & Eby, M. 1996 Effects of topographic stress on Caribbean Sea circulation. *J. Geophys. Res.* **101**, 16449–16453.

Treguier, A. M. 1989 Topographically generated steady currents in barotropic turbulence. *Geophys. Astrophys. Fluid Dyn.* **47**, 43–68.

Treguier, A. M. & McWilliams, J. C. 1990 Topographic influences on wind-driven, stratified flow in a beta-plane channel: An idealized model of the Antarctic Circumpolar Current. *J. Phys. Oceanogr.* **20**, 321–343.

Vallis, G. K. & Hua, B.-L. 1988 Eddy viscosity of the anticipated potential vorticity method. *J. Atmos. Sci.* **45**, 617–627.

Zou, J. & Holloway, G. 1994 Entropy maximization tendency in topographic turbulence. *J. Fluid Mech.* **263**, 361–374.